“© 2017 IEEE. Personal use of this material is permitted. Permission from IEEE must be obtained for all other uses, in any current or future media, including reprinting/republishing this material for advertising or promotional purposes, creating new collective works, for resale or redistribution to servers or lists, or reuse of any copyrighted component of this work in other works.”

Simplified Tightly-Coupled Cross-Dipole Arrangement for Base Station Applications

Can Ding, *Member, IEEE,* Haihan Sun, *Student Member, IEEE,*
Richard W. Ziolkowski, *Fellow, IEEE,* and Y. Jay Guo, *Fellow, IEEE*
.

***Abstract*—The electromagnetic fundamentals that govern the performance characteristics of dual-polarized tightly-coupled cross-dipoles that are widely used in cellular base station applications are investigated. The mutual coupling effects and their impact on standard performance indices are stressed. A model is developed that considers this type of cross-dipole as an array. Links between the physical dimensions of the components of this model and key radiation characteristics, including directivity, half-power-beamwidth (HPBW), and cross polarization discrimination (XPD) levels, are established. The model guides the introduction and optimization of a simplified cross-dipole structure that exhibits excellent performance. A prototype was fabricated, assembled, and tested. The measured results are in good agreement with their simulated values, validating the model and its governing principles.**

***Index Terms*—Arrays, base station antenna, cross-dipole antennas, dual-polarization, tightly-coupled elements.**

I. Introduction

OUR daily lives have benefited significantly from the development of wireless communication technologies. Modern mobile systems provide us with not only communications, but also other applications such as internet connectivity, bio monitoring, activity tracking, video conferencing, and even virtual reality. The upcoming 5th generation (5G) wireless communication systems promise even more revolutionary technologies to the benefit of our daily lives, including home service robotics and autonomous cars.

One of the initial major challenges to building 5G wireless communication systems will be the need to integrate future 5G antennas with existing 3G/4G antenna platforms. This near-term complication will engender more stringent requirements on base station antennas, i.e., they must be able to manage these more complicated electromagnetic environments. As a consequence, it is now becoming imperative for the mobile industry to develop new antenna technologies to address the challenges in deploying 5G base stations antennas. However, without any regulatory standards for them in place, the most effective starting point in preparation for future 5G developments is a more thorough investigation of the operating principles that govern current base station antennas on 3G/4G platforms.

Manuscript submitted 03 Oct. 2017. This work was funded by Australian Research Council (ARC) DP160102219

All the authors are with the Global Big Data Technologies Centre (GBDTC), University of Technology Sydney (UTS), Sydney, NSW, 2121, Australia. e-mail:(can.ding@uts.edu.au)

Richard W. Ziolkowski is also with the Department of Electrical and Computer Engineering, The University of Arizona, Tucson, AZ 85721 USA. Email: ziolkows@email.arizona.edu.

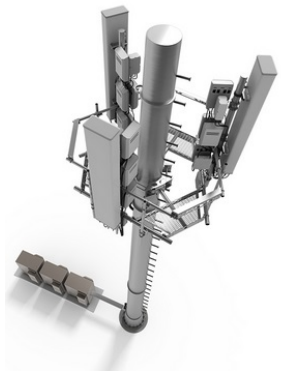

Fig. 1. Configuration of a typical base station array for cellular coverage.

Base station antennas for current 2G/3G/4G platforms are designed to provide dual-polarizations of ±45° to enhance the system capacity and to combat the multipath propagation effects. To provide a full coverage of a geographic area, usually 3 arrays are employed to have an omnidirectional pattern in the horizontal plane and a narrow beam in the vertical plane. A typical example is shown in Fig. 1. The antenna elements used in this configuration are required to be able to maintain stable radiation performance in the target band. Commonly used industry specifications for the antennas in this configuration are:

- VSWR < 1.5
- Half-Power Beamwidth (HPBW) in the horizontal plane: 65° ± 5°
- Polarization ±45°
- Cross Polarization Discrimination (XPD):
  - ····· at boreside in the horizontal cut > 20 dB
  - ····· within ±60° in the horizontal cut > 10 dB
- Front-Back-Ratio (FBR): > 20 dB
- Port Isolation: > 25 dB

Note that the horizontal cut refers to the xz-plane of the antenna elements illustrated in Fig. 2. Current wireless cellular communication systems employ several frequency bands for 2G/3G/4G applications, including GSM700 (698-793 MHz), GSM850 (824-894 MHz), GSM900 (880-960 MHz), DCS (1.71-1.88 GHz), PCS (1.85-1.99 GHz), UMTS (1.92-2.17 GHz), LTE2300 (2.3-2.4 GHz), and LTE2500 (2.5-2.69 GHz). Base station antenna arrays that can cover all of these bands

are preferred since they can be used in multiple applications. However, to guarantee a good radiation performance, a lower band from 698 to 960 MHz (31.6%) and a higher band from 1710 to 2690 MHz (44.5%) are covered separately by two different antenna arrays. We note that it is still a great challenge for the array covering the higher band to meet all of the specifications.

There are various types of antennas targeted at these base station applications in the literature, including patch antennas [1, 2], magneto-electric dipoles [3, 4], slot antennas [5], and cross-dipoles [6–16]. However, only a few can actually meet all of the commercial requirements. Among them, cross-dipoles continue to be the most promising solutions and have gained significant popularity in industry. Fig. 2(a) to 2(g) illustrates some cross-dipoles reported in the literature [7–13]. A dual-polarized cross-dipole consists of a pair of sub-dipoles oriented perpendicular to each other. By exciting either one of the two sub-dipoles, different polarizations can be obtained. Primitive cross-dipoles have their two sub-dipoles "isolated" from each other, like the designs shown in Fig. 2(a) and 2(b). These "isolated" configurations have limited bandwidth. For example, the antennas shown in Fig. 2(a) and 2(b) only have an impedance bandwidth of 5% and 23.7%, respectively [7, 8]. The design shown in Fig. 2(a) was improved [14] by adding some directors to have a wider bandwidth, 12.5%. However, the bandwidth achieved from these "isolated" cross-dipoles is far from satisfactory; it does not come close to covering the higher-band bandwidth requirement of 44.5%.

More recently, cross-dipoles that have their sub-dipoles closely spaced and tightly coupled to each other, as shown in Figs. 2(c) to 2(g), have been advocated. By optimizing the mutual coupling between the two sub-dipoles, both can be activated when only one of them is excited. This behavior leads to a significant improvement of the impedance bandwidths. For example, all the reported antennas shown in Figs. 2(d) to 2(g) [10–13, 15, 16] have their bandwidths > 44.5% with their VSWR < 1.5. Moreover, one finds that a stronger coupling between the sub-dipoles may also increase the gain. For example, the cross-dipoles shown in Figs. 2(d) to 2(f) exhibit stronger couplings and, hence, have gains that are about 1.0 dB higher on average than the weaker coupling design shown in Fig. 2(g), which exhibits gains ranging from 7 to 8.6 dBi.

While it is known that the coupling between the sub-dipoles can increase the impedance bandwidth and perhaps enhance the radiation performance, the fundamental understanding of why it facilitates these effects is still superficial. There is no clear methodology available currently to guide the optimization of the coupling to achieve the best performance. This article will reveal a deeper understanding of how inter-element coupling expedites the cross-dipole performance enhancements and will provide the linkages between the physical dimensions of its elements, the current distributions on them, and the performance indices of concern to industry. The cross-dipole models are presented in Section II. The coupling analysis is discussed in Section III. Tightly-coupled arrays are considered in Section IV. The analysis and simulation efforts associated with both of these issues, which were substantial, led to an optimized tightly-coupled cross-dipole system that has a very simple structure, but excellent performance characteristics. This optimized design is introduced in Section V. As will be described in Section VI, a prototype was fabricated and tested. The measured results are demonstrated to be in good agreement with their simulated values.

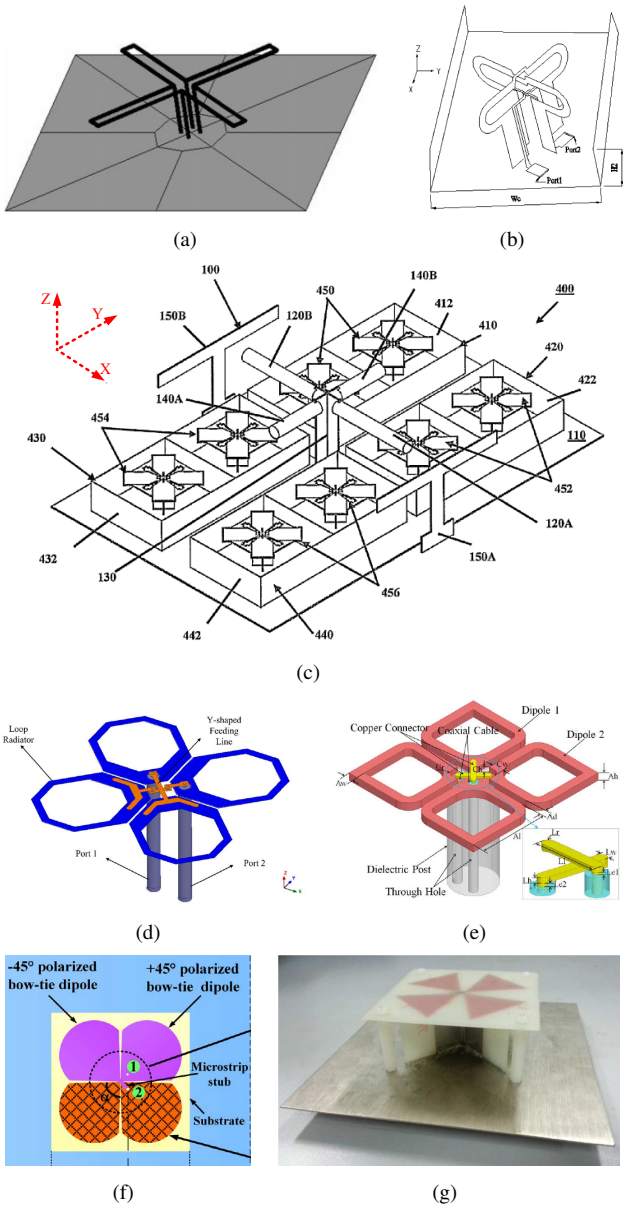

Fig. 2. Configurations of dual-polarized cross-dipoles developed for base station applications reported in the literature. (a) Ref [7]. (b) Ref [8]. (c) Ref [9]. (d) Ref [10]. (e) Ref [11]. (f) Ref [12]. (g) Ref [13].

II. Model Description

The analysis in this work is based on a cross-dipole with a typical configuration as shown in Fig. 3(a). It consists of two identical sub-dipoles placed perpendicular to each other. Square-looped dipole arms are employed in order to have a larger aperture to get more bandwidth and gain. The traces constructing the square-looped arms have length L and width W. The square-looped arms are placed close to each other and separated by a small distance s. This choice enables the

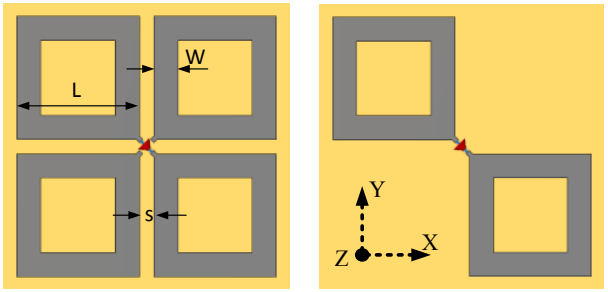

(a) (b)

Fig. 3. Cross-dipole geometry. (a) Model-A: tightly-coupled cross dipoles consisting of a driven dipole and a parasitic dipole. (b) Model-B: driven dipole only.

strong coupling between the elements. The dipoles are printed on a Rogers 4530B substrate whose relative permittivity and permeability are, respectively, 3.55 and 1.0; loss tangent is 0.0027; and thickness is 1.524 mm. The active dipole is shown in Fig. 3(b). The other dipole is a parasitic element. The traces between the square loops have a 0.3 mm width.

The analysis is conducted within the frequency band from 1.7 to 2.7 GHz, which covers the base station operational band from 1710 to 2690 MHz. The data used for the theoretical analysis are obtained from a simulation model which does not include the presence of the balun and the matching circuit. The balun and matching circuit are only used to facilitate impedance matching and a balanced feed. This model choice simplifies the computational effort; it is very reasonable because the matching circuit will be shielded by the balun in reality and a well-designed balun only has minor currents on its outer surface. Consequently, the latter will have only a very minor effect on the radiation performance. The theoretical model thus leads to an optimized cross-dipole structure that provides a satisfactory assessment of the radiation performance and impedance bandwidth. The balun and matching circuit are then added back into the optimized theoretical design, and the cross-dipole system is re-optimized to achieve impedance in the target band.

III. Coupling Analysis

By exciting the driven dipole shown in Fig. 3(b), the parasitic dipole included in Fig. 3(a) can also be activated because of the coupling between them. To determine how the coupling changes the overall performance, the driven dipole was simulated by itself. The differences between the results of these two models were then obtained. The model with and without the parasitic dipole is denoted as Model-A and Model-B, respectively. The traces in Model-A and Model-B had the same dimensions (L= 25.5 mm, W = 6.0 mm, s = 3.0 mm). Their dipole elements were placed above a square reflector at a vertical distance of h = 32.0 mm. The size of this square reflector was $160 \times 160\ mm^2$. These design parameter values were selected to facilitate having the resulting idealized cross dipole system work properly in the target band.

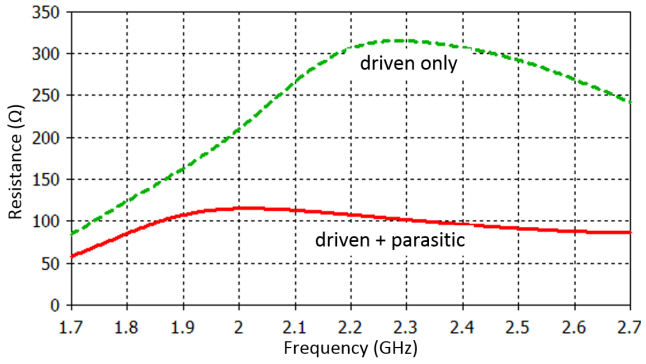

(a)

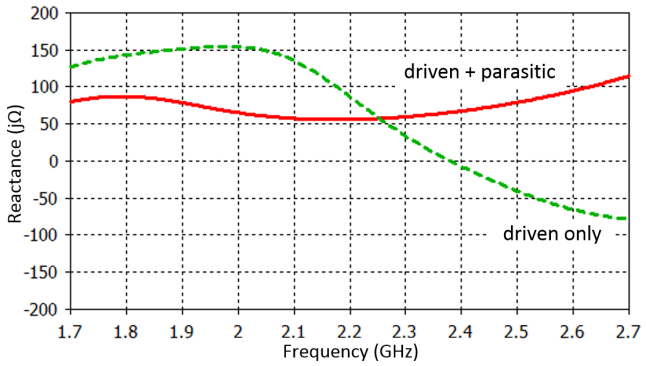

(b)

Fig. 4. Variations of the impedance of Model-A and Model-B in the target band. (a) Resistance. (b) Reactance.

A. Impedance

Fig. 4(a) and 4(b) shows the variations of the resistance and reactance, respectively, of Model-A and Model-B across the design frequency band. It is observed that the fluctuations in both the resistance and the reactance are smaller with the presence of the parasitic dipole. This behavior indicates that the parasitic dipole alleviates the impedance variation of the driven dipole, making it easier to match the system to a real source within the design band. This also leads to an increase in the system bandwidth, an outcome expected because of the large sizes of both sub-dipoles needed to achieve operation in it.

B. Radiation Performance

Comparisons of the main radiation performance indices of interest are listed in Table I. It is clear that the coupling between the driven and parasitic dipoles offers a higher directivity, a narrower HPBW, and a higher XPD within ±60° of the z-axis in the horizontal plane cut (xz-plane). To have a better understanding of what causes these enhancements, the current distributions within the apertures of both models are depicted in Figs. 5(a) and 5(b). It is observed that the driven dipole exhibits the standard behavior with or without the coupling, i.e., the peaks of the current distributions occur near the excitation source and the valleys are located at the ends of the dipole arms. On the other hand, the parasitic dipole has a different current distribution since it is excited by the

TABLE I
COMPARISON OF THE RADIATION PERFORMANCE OF MODEL-A AND MODEL-B

	A: driven+parasitic	B: driven only
Directivity (dBi)	8.6 - 9.3	8.5 - 9
HPBW (°)	63 - 69	65 - 75
XPD@0° (dB)	> 50	> 50
XPD@60° (dB)	9 - 11	7 - 11

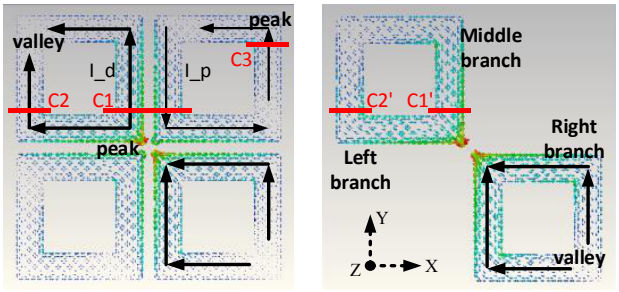

(a) (b)

Fig. 5. Current distributions on the traces of the models. (a) Model-A. (b) Model-B.

capacitive coupling between the parallel branches of the two sub-dipoles.

The currents were monitored on several branches of the dipoles and as a pair of adjacent branches. One observed feature was that the induced current I_p and the driven current I_d are out of phase. This phenomenon is interesting since a reverse current should theoretically reduce the directivity, but the realized directivity is even higher. In order to explain this dichotomy, the trace current monitors: C1, C2, C3, C1' and C2', were located as shown in Fig. 5. They are placed near the peaks of the current distributions on the individual branches. Due to the diagonal symmetry of the aperture, the current distributions on the x- and y-aligned branches are identical. Therefore, only the y-aligned currents were monitored and analyzed. Moreover, the y-aligned currents on the left-, middle-, and right branches work together to produce field contributions analogous to a 3-element dipole array. This aspect facilitated explaining the results. The magnitudes and phases of the currents within the entire frequency band were obtained.

The current magnitudes on the middle branches of the two models at C1 and C1' are compared in Fig. 6(a). Their values on the left branches at C2, C2' and those on the right branch at C3 are compared in Fig. 6(b). First, notice that the magnitudes of the total current (I_d - I_p) on the middle branch with or without the coupling are at the same level (i.e., C1≈C1'). Although the coupling introduces a reverse current I_p on the parasitic dipole, an increase of the current density on the driven dipole I_d compensates for it. Hence, there is no reduction in the directivity. Second, notice that the currents on the left-most branch of the driven dipole with or without the coupling also remain at a similar level (i.e., C2≈C2'). Third, notice that there is additional current (C3) induced on the top right branch of the parasitic element and it has a magnitude comparable to the driven current on the left branch (i.e., C3 is comparable with

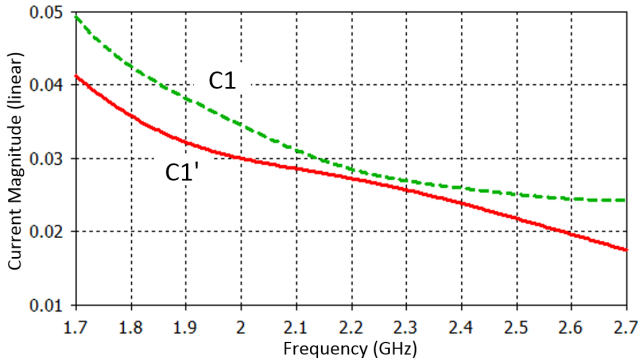

(a)

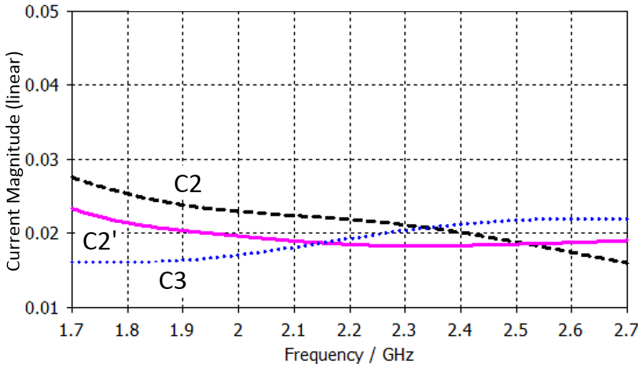

(b)

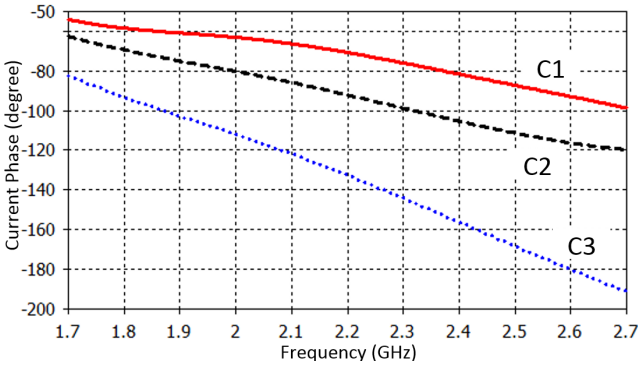

(c)

Fig. 6. Simulated currents. (a) Current magnitude on the middle branches of Model-A and Model-B. (b) Current magnitudes on the side branches of Model-A and Model-B. (c) Current phases on three different branches of Model-A.

C2). Finally, the phases of the currents on the left-, middle-, and right-branches of Model-A are plotted in Fig. 6(c). The phase differences between these currents are < 90° within the entire band. Therefore, the contributions to the radiated field from the three y-aligned currents add coherently on boresight. The outcome is the fact that a higher directivity and a narrower HPBW are obtained from this cross-dipole system.

The XPD is another crucial factor used to assess the radiation performance of a base station antenna. For cellular coverage applications, the value of the XPD along the bore-sight direction (θ = 0°, point A in Fig. 7) is required to be > 20 dB, and the minimum XPD within the entire set of coverage angles ($-60° < \theta < 60°$, points B and B' in Fig. 7) has to be > 10 dB. Usually, the worst XPD occurs at the bandwidth edges.

In a majority of cases, the condition that the XPD@0° > 20 can be satisfied. However, to maintain the XPD@±60° > 10 dB within the entire operation band is a challenge. For example, the calculated XPD@±60° for Model-B is from 7-11 dB over that band.

In order to achieve a higher XPD in base station antenna designs, one must start by investigating what contributes to it. Grasping the impact of this performance factor can be confusing because one normally looks at the ±45° polarization vectors in the xz-plane cut ($\phi = 0°$) rather than in the $\phi = 45°$ cut. To examine its meaning, consider the electric field that is generated by the cross-dipole antenna as shown in Fig. 7. The far-field x- and y-components can be expressed as:

$$\hat{x} \cdot \vec{E} = E_x e^{j\phi_x},\ \hat{y} \cdot \vec{E} = E_y e^{j\phi_y} \tag{1}$$

which is commensurate with the presence of the already identified x- and y-aligned currents in Fig. 5(a). Then the co- and cross-polarized field vectors in the $\phi = \pm 45°$ cut planes take the form:

$$\begin{aligned} E_{co} &= cos\frac{\pi}{4}E_x e^{j\phi_x} + cos\frac{\pi}{4}E_y e^{j\phi_y}, \\ E_{cross} &= cos\frac{\pi}{4}E_x e^{j\phi_x} - cos\frac{\pi}{4}E_y e^{j\phi_y}. \end{aligned} \tag{2}$$

The XPD is the ratio of the co- and cross-pol magnitudes:

$$\begin{aligned} XPD = \left|\frac{E_{co}}{E_{cross}}\right| &= \sqrt{\frac{E_x^2 + E_y^2 + 2E_xE_ycos(\phi_x - \phi_y)}{E_x^2 + E_y^2 - 2E_xE_ycos(\phi_x - \phi_y)}} \\ &= \sqrt{\frac{1+M}{1-M}}, \end{aligned} \tag{3}$$

where

$$M = \frac{2E_xE_ycos(\phi_x - \phi_y)}{E_x^2 + E_y^2}. \tag{4}$$

Note that if one observes the fields at a point infinitely far away from the antenna aperture, both the E_x and E_y components arrive at essentially the same time, which means $\phi_x = \phi_y$. Therefore, the term M can be written to a very good approximation as

$$M = \frac{2E_xE_y}{E_x^2 + E_y^2} = \frac{2}{\frac{E_x}{E_y} + \frac{E_y}{E_x}}. \tag{5}$$

Then to connect the XPD value to the field components most naturally generated by the currents on the antenna elements, we define

$$XPD' = \frac{E_x}{E_y}. \tag{6}$$

as the cross polarization discrimination factor between the x- and y-polarized far-field components. Then the actual XPD factor can be expressed as

$$XPD = \left|\frac{XPD' + 1}{XPD' - 1}\right|. \tag{7}$$

Consequently, it is now clear that in order to obtain a larger XPD as required for base station applications, XPD' should be as close to 1 as possible. In other words, we have to optimize the antenna to maintain the difference between the magnitudes of the generated x- and y-polarized radiation to be as small as possible in the xz-plane cut across the entire operational band.

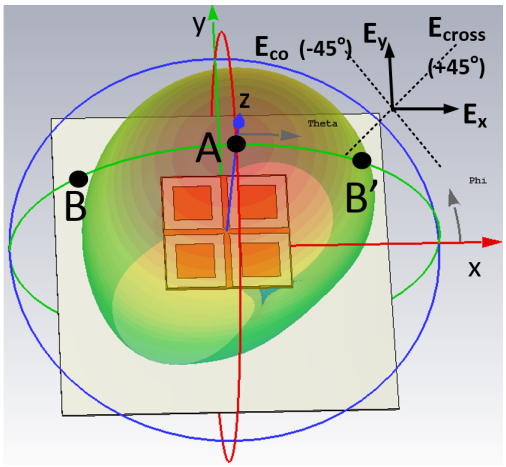

Fig. 7. Schematic 3D radiation pattern of the proposed tightly-coupled cross-dipole.

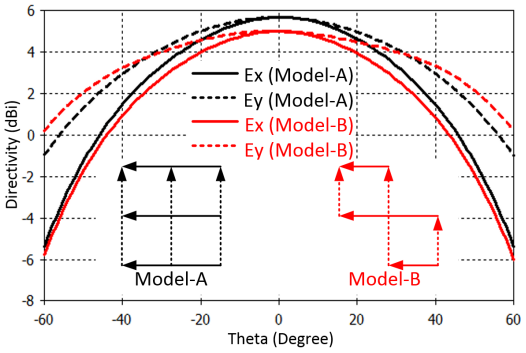

Fig. 8. Comparison of x- and y-aligned radiation patterns of Models-A and -B.

Fig. 8 compares the x- and y-polarized radiation patterns generated with Model-A and Model-B in the xz-plane cut. A strictly diagonal, symmetric structure relative to the boresight direction would ensure that $E_x = E_y$ and, hence, would produce an infinitely high XPD@0°. As shown, this is true for both models. However, the symmetry in a real environment is difficult to ensure and the ratio of the field components may deteriorate some from unity, resulting in a lower XPD. For example, a radome used to cover a base station antenna may scatter differently in the x- and y-directions, which leads to a broken symmetry and a decreased XPD at boresight.

Note that this symmetry generally no longer exists at the edges of the coverage directions, i.e., when $\theta \sim \pm 60°$. As illustrated in Fig. 8, although both E_x and E_y are getting smaller as θ varies from 0° to ±60°, E_x (solid lines) decreases faster than E_y (dashed lines). This behavior is more noticeable for the non-symmetric Model-B. Although the x- and y-aligned currents are nearly the same, the asymmetry of the overall structure causes the patterns in the E-plane (horizontal cut, xz-plane) and H-plane (vertical cut, yz-plane) to be different. Moreover, one finds this asymmetry also leads to a more severe narrowing of the patterns in both planes. In contrast, the more symmetric Model-A, in which the parasitic

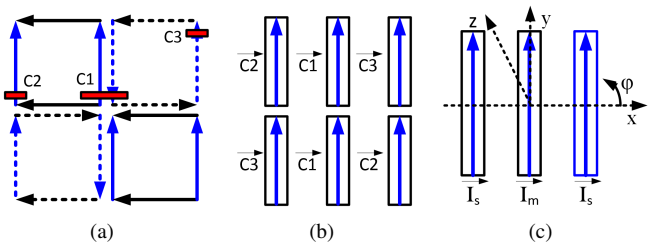

Fig. 9. Representation of the current distributions. (a) Schematic for the tightly-coupled cross-dipole antenna. (b) Equivalent six-element dipole array for model-A. (c) Reduced, equivalent three-element dipole array model.

sub-dipole is excited by the mutual coupling effects, leads to more stable and less narrowing of the E- and H-plane patterns and to a larger XPD across the entire coverage range.

IV. TIGHTLY-COUPLED CROSS-DIPOLE ANTENNA DESIGN METHODOLOGY

To more closely tie the design parameters to its performance characteristics, we have developed an analytical array model of the tightly-coupled cross-dipole antenna. This model and a parameter study based on it provide further insights into how the system achieves low VSWR, stable HPBW, and high XPD across the coverage range and the operational bandwidth.

A. Array Model

Fig. 9(a) presents a schematic of the current distributions on the cross-dipole aperture. The solid and dashed arrows denote the directly-excited currents and the induced parasitic currents, respectively. To develop the array model, only the y-aligned currents are considered. An analogous model can be developed in the same manner for the x-aligned currents.

The three current monitors C1, C2, and C3, identified previously, monitor the magnitudes and phases at the peaks of their distributions. Due to the observed symmetries, there are only three unique current vectors on the aperture:

$$\begin{aligned} \overrightarrow{C1} &= C1e^{j\phi_1}, \\ \overrightarrow{C2} &= C2e^{j\phi_2}, \\ \overrightarrow{C3} &= C3e^{j\phi_3}. \end{aligned} \tag{8}$$

They are identified in Fig. 9(b). Although these three current vectors have different magnitudes and phases, they all actually have similar quarter-period quasi-sinusoidal magnitude distributions and small phase differences $< 90°$ as long as the size of the cross-dipole system is reasonable (i.e., the side length of the aperture is near a quarter-wavelength). Therefore, we can merge the current vectors on the six branches of the model depicted in Fig. 9(b) into the three dipole current vectors shown in Fig. 9(c).

Next, because the detected currents on the outside branches of the three-element array are the same, the currents on their equivalent dipoles will be denoted by the vector $\overrightarrow{I_s}$. The current on the equivalent center dipole is then denoted by the vector $\overrightarrow{I_m}$. From the Model-A simulation data it is found that the currents $\overrightarrow{I_m}$ and $\overrightarrow{I_s}$ have identical half-period quasi-sinusoidal current directions, to be denoted as $\overrightarrow{I_0}$. Thus, they can be represented as

$$\begin{aligned} \overrightarrow{I_s} &= \overrightarrow{I_0}(C3e^{j\phi_3} + C2e^{j\phi_2})/2, \\ \overrightarrow{I_m} &= \overrightarrow{I_0}C1e^{j\phi_1}, \end{aligned} \tag{9}$$

where $\overrightarrow{I_s}$ is the combination of the branch currents C2 and C3, as depicted in Fig. 9.

The radiation pattern generated by these three y-polarized current elements can be represented as

$$F_y(\theta,\phi) = AF(\theta,\phi) * f_0(\theta,\phi), \tag{10}$$

where $AF(\theta,\phi)$ is the three-element array factor and $f_0(\theta,\phi)$ is the radiation pattern of a dipole element. The corresponding radiation pattern, $F_x(\theta,\phi)$, that is generated by the analogous x-oriented three-element dipole array model has the same form. Consequently, it can be related to $F_y(\theta,\phi)$ by a simple rotation, i.e., as:

$$F_x(\theta,\phi) = F_y(\theta,\phi+90°). \tag{11}$$

Therefore, combining the fields radiated by both the x- and y-aligned currents, the total radiation pattern is:

$$\begin{aligned} F(\theta,\phi) &= F_x(\theta,\phi) + F_y(\theta,\phi) \\ &= F_y(\theta,\phi+90°) + F_y(\theta,\phi). \end{aligned} \tag{12}$$

The xz-cut of this radiation pattern is

$$\begin{aligned} F(\theta,\phi=0) &= F_y(\theta,\phi=0°) + F_y(\theta,\phi=90°) \\ &= AF(\theta,\phi=0°) * f_0(\theta,\phi=0°) \\ &+ AF(\theta,\phi=90°) * f_0(\theta,\phi=90°) \\ &= AF(\theta,\phi=0°) * f_H(\theta) + AF(\theta,\phi=90°) * f_E(\theta) \end{aligned} \tag{13}$$

where $f_H(\theta)$ and $f_E(\theta)$ represent the H- and E-plane patterns of the dipole oriented along $\overrightarrow{I_0}$. Because the y-aligned currents are spaced along the x-axis, the array factor along the y-axis is identically equal to 1.0, i.e.,

$$AF(\theta,\phi=90°) \equiv 1. \tag{14}$$

Therefore, the cross-dipole's radiation pattern in the xz-cut (13) can be rewritten as

$$F(\theta,\phi)|_{\phi=0°} = AF(\theta,\phi=0°) * f_H(\theta) + f_E(\theta). \tag{15}$$

where AF_H is the three-dipole element array factor in the dipole's H-plane. The first and second terms in this expression represent the contributions from the x- and y-aligned dipole currents, respectively.

From Eq. (6) one then has

$$XPD' = AF_H * f_H/f_E \tag{16}$$

and the XPD factor from Eq. (7) becomes:

$$XPD(\theta) = \left|\frac{XPD'(\theta)+1}{XPD'(\theta)-1}\right| = \left|\frac{f_E(\theta)+AF_H(\theta)f_H(\theta)}{f_E(\theta)-AF_H(\theta)f_H(\theta)}\right| \tag{17}$$

Therefore, it is concluded that the radiation performance characteristics, XPD and HPBW, are determined simply with the array factor $AF_H(\theta)$ and the dipole's E- and H-plane patterns, $f_E(\theta)$ and $f_H(\theta)$. Consequently, when the physical

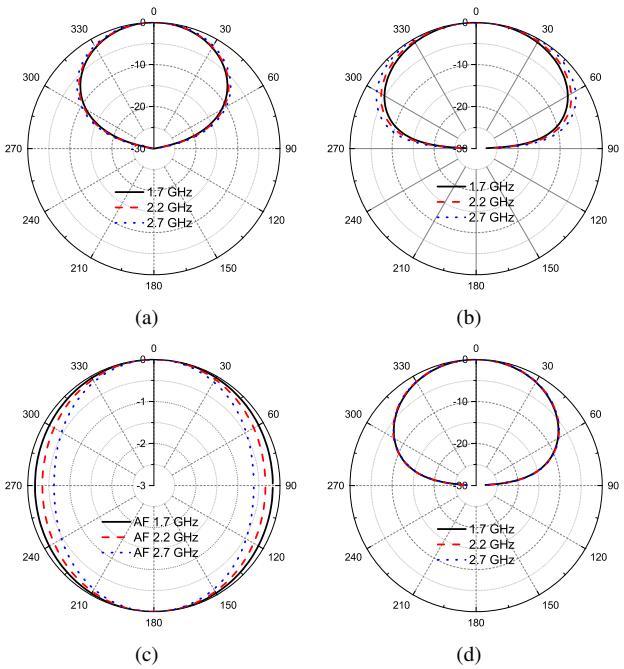

Fig. 10. Simulated radiation patterns. (a) E-plane pattern and (b) H-plane pattern of a single half-wavelength dipole placed a quarter-wavelength above an infinite ground plane and oriented parallel to it. (c) Three-element array factor pattern alone. (d) Model-A-based cross-dipole radiation pattern.

dimensions of the cross-dipole antenna are being optimized, one is equivalently manipulating the array factor and the radiation patterns of the array elements.

From equation (9) and Fig. 9(c), the three-element dipole array factor is calculated as:

$$\begin{aligned} AF(\theta) &= \left| \sum_{n=1}^{3} W_n e^{-jk\cdot r_n} \right| \\ &= |A_s I_0 e^{j\phi_s} e^{jk(-d)cos(\theta)} + A_m I_0 e^{j\phi_m} e^{j0} \\ &+ A_s I_0 e^{j\phi_s} e^{jk(d)cos(\theta)}| \\ &= |I_0 e^{j\phi_m}[A_s e^{j(\phi_s-\phi_m)}(e^{-jkdcos\theta} + e^{jkdcos\theta}) + A_m]| \\ &= I_0|2A_s cos(kdcos\theta)e^{j(\Delta\phi)} + A_m| \\ &= I_0\{[2A_s cos(kdcos\theta)cos(\Delta\phi) + A_m]^2 \\ &+ [2A_s cos(kdcos\theta)sin(\Delta\phi)]^2\}^{\frac{1}{2}} \end{aligned} \tag{18}$$

where $k = 2\pi/\lambda$, $\Delta\phi = \phi_s - \phi_m$, and d is the separation distance between the dipole elements. The array factor is thus calculated straightforwardly once the magnitudes and phases of the currents are obtained from the monitors C1, C2, and C3.

Figs. 10(a) and 10(b) show the E- and H-plane radiation patterns, $f_E(\theta)$ and $f_H(\theta)$, respectively, of a straight half-wavelength dipole placed a quarter-wavelength above a ground plane and oriented parallel to it for several source frequencies. To eliminate the effect of the ground plane's size, it is set to be infinitely large. It is observed from these two sub-figures that a typical dipole placed above a reflector has its H-plane pattern getting wider and its E-plane pattern being relatively stable as the frequency increases. Fig. 10(c) plots the array factor patterns of Model-A alone in free space. Fig. 10(d) plots the corresponding cross-dipole array patterns calculated from (15) at the same frequencies. These composite patterns are very stable across the target band. It is clear that along with the stable E-plane patterns, the array factor variations with frequency nicely compensate for the variations in the H-plane patterns, resulting in very stable overall patterns.

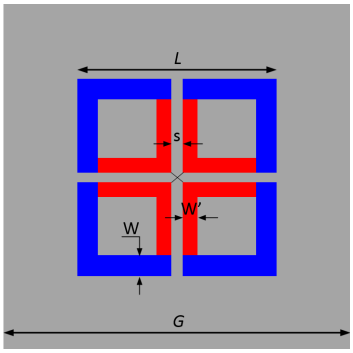

Fig. 11. Revised and simplified cross-dipole configuration.

B. Parameter Analysis

The array model analysis theoretically demonstrated why a stable radiation pattern can be realized across a wide band with a cross-dipole configuration. Because only the E- and H-plane patterns of the equivalent dipole elements and the H-plane array factor determined the overall pattern, there are methods available to engineer these key factors. These include:

- E-plane pattern of a dipole above a reflector $f_E(\theta)$: Dipole length; distance away from the reflector; reflector size.
- H-plane pattern of a dipole above a reflector $f_H(\theta)$: Distance away from the reflector; reflector size.
- H-plane array factor $AF_H(\theta)$: Shape of the array element, which changes the amplitude and phase distributions on it (e.g., adding a slot/stub to or bending it can result in a different array factor); separation distance between the array elements.

These methods are employed to optimize the design of the simplified, practical cross-dipole model illustrated in Fig. 11. The adjustable parameters are the aperture length L, outside branch width W (black branches), inside branch width W' (grey branches), gap width s, antenna height h, and ground plane reflector size G. It is noted that any of these parameters and any of their combinations can affect the radiation patterns. Furthermore, some of these parameters are also critical for impedance matching. To obtain a cross-dipole system that meets all of the design specifications, it is very helpful to know how each parameter impacts the overall performance. A variety of parameter sweeps were investigated. During each sweep, only one of these design parameters was allowed to vary and the others were fixed to the values listed in Table II. These tabulated dimensions are their optimized values, which were obtained with an exhaustive set of simulations, and are the ones used for the fabrication of the prototype antenna.

TABLE II
OPTIMIZED DIMENSIONS OF THE SIMPLIFIED CROSS-DIPOLE ANTENNA (DIMENSIONS IN MILLIMETERS)

Parameter	Value	Description
L	60.0	Aperture length
W	5.5	Width of the outside branches
W'	4.0	Width of inside branches
s	5.4	Distance between inside arms
h	33.0	Antenna height
G	160.0	Ground plane length

Figs. 12 and 13 illustrate how each design parameter affects the HPBW and the input impedance of the cross-dipole system. Only the HPBW results are presented in Fig. 12 since it is a key coverage parameter and whatever impacts it will also affect the other radiation performance characteristics such as the XPD and gain. The input impedance results given in Fig. 13 are obtained for the cross-dipole elements placed above the reflector, but with no feed network being present.

As shown in Fig. 12(a), the HPBW varies significantly with the aperture length L. This is attributed to the fact that L is closely related to the array factor $AF_H(\theta)$ and $L/2$ is the separation distance between the array elements. A larger L results in a more directive $AF_H(\theta)$, and thus a narrower HPBW. At the same time, L is also a key parameter for tuning the input impedance as shown in Fig. 13(a).

Figs. 12(e) and 12(f) show that the HPBW also changes with the antenna height h and the ground plane reflector size G. These larger variations are associated with the fact that h and G critically impact the dipole radiation patterns $f_E(\theta)$ and $f_H(\theta)$. However, they do not affect the couplings that occur between the elements in the aperture. Consequently, they do not affect the array factor $AF_H(\theta)$. Moreover, as long as they are changed in reasonable ranges, they do not affect the input impedance. This feature is illustrated in Figs. 13(e) and 13(f).

As shown in Figs. 12(b), 12(c), and 12(d), the remaining parameters: s, W, and W', only demonstrate minor abilities to aid in the tuning of the HPBW. This fact is easy to understand since the radiation pattern of a dipole is much more closely related to its length rather than to its widths. On the other hand, optimizing those widths and the coupling distance between the dipole branches is critical for realizing good impedance matching. The parameter sweep results shown in Figs. 13(b), 13(c), and 13(d) prove the fact that these parameters have a definite impact on the input impedance tuning.

C. Discussion

The presented analysis and results demonstrate that the tightly-coupled cross-dipole configuration addressed in this work can be decomposed into two arrays, an x-aligned and a y-aligned 3-element dipole array placed above a ground plane reflector. The radiation pattern was determined to be given by two factors: the E- and H-plane patterns of the dipole element and its ground plane image, and the bare H-plane array factor. Because with increasing frequency the patterns associated with the dipole (pattern widens) and array factor (pattern narrows) have compensating effects, high pattern and, hence, high XPD consistency can be achieved across the entire operational band.

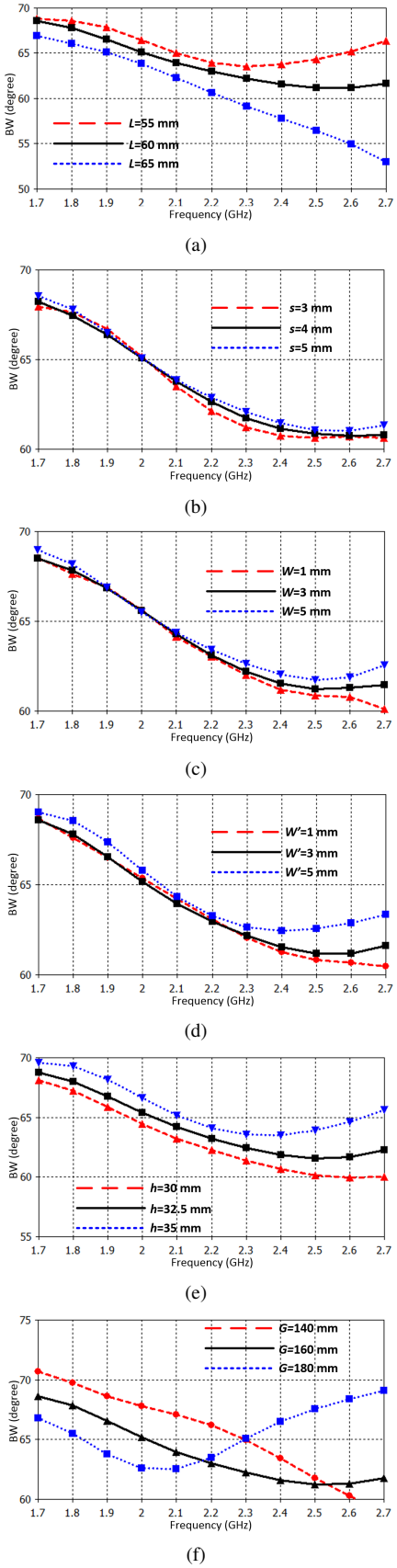

Fig. 12. HPBW plotted on the Z-Smith diagram for the parameters: (a) L, (b) s, (c) W, (d) W', (e) h, and (f) G.

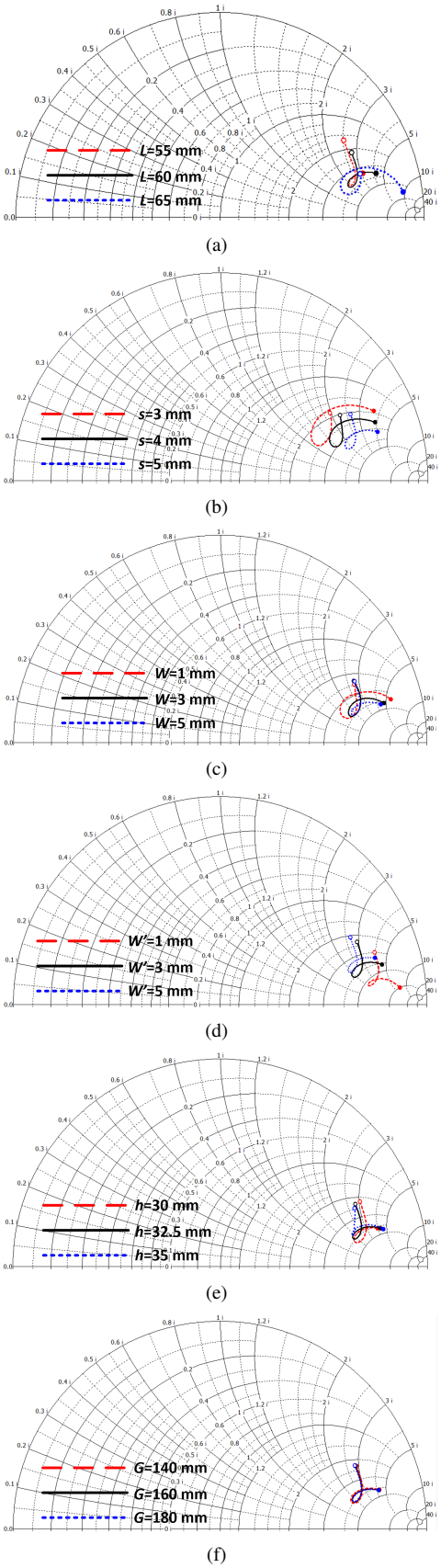

Fig. 13. Input impedance plotted on the Z-Smith diagram for the parameters: (a) L, (b) s, (c) W, (d) W', (e) h, and (f) G.

The imaging effects, of course, can be controlled by the reflector's size G and the distance h between dipole elements and reflector. They have a significant effect on the radiation pattern but only a minor effect on the input impedance. The array factor is a much more important factor for the radiation performance, especially for the XPD. However, as shown in Fig. 11, it is not easy to adjust the array factor because of competing effects. Changing L can change the array factor, but it also affects the impedance matching. A more appropriate and practical method to change the array factor is to introduce parasitic elements. Equivalently, this introduces more array elements, resulting an array factor that can be engineered. For example, the practical design shown in Fig. 2(c) employ walls surrounding the high band elements and two parasitic dipoles for the low band elements to shape the system's output beams.

Based on the identified features of the equivalent dipole array model, the following design procedure is advocated. First, the design dimensions L, h, and G should be determined to yield a satisfactory radiation performance. We have employed the commercial software environment CST Microwave Studio (MWS) for these simulation parameter studies. The antenna height h and reflector size G should be kept as small as possible to guarantee a compact structure. Parasitic elements should be considered to better shape the beam if necessary. Second, the design parameters s, W, and W' should be optimized to facilitate good input impedance matching. To determine whether the realized cross-dipoles can be matched in the target band, one can export the MWS S1p file representing the input impedance. One can then connect it with an idealized matching circuit in the MWS circuit simulator as shown in Fig. 14(c) to optimize the system. This matching method, as described in [17], is an optimal way to match the dipole antennas to the feed network and readily leads to a printed circuit board (PCB) implementation. Subsequently, a physical matching circuit can be designed from the resulting optimized circuit theory model. Finally, if needed, minor overall adjustments can be made to the overall design to achieve excellent impedance matching performance.

V. Antenna Design

It was desired to fabricate and test a prototype of our simplified cross-dipole antenna. Following our design procedure, the basic structure and its radiation performance were obtained. A matching circuit was then designed to facilitate its realization. Then, the combined antenna and matching circuit were optimized together to achieve the final prototype design.

A. Matching

The ideal cross-dipole structure shown in Fig. 11 together with the ground plane reflector were firstly optimized numerically to have a good radiation performance. As noted for the idealized system, the structure was designed to be printed on a Rogers 4530B substrate. The optimized dimensions of the structure are those listed in Table II. The next step was to design the matching network.

As shown in Fig. 14(a), two feed networks, one for each sub-dipole, are placed perpendicular with each other and to

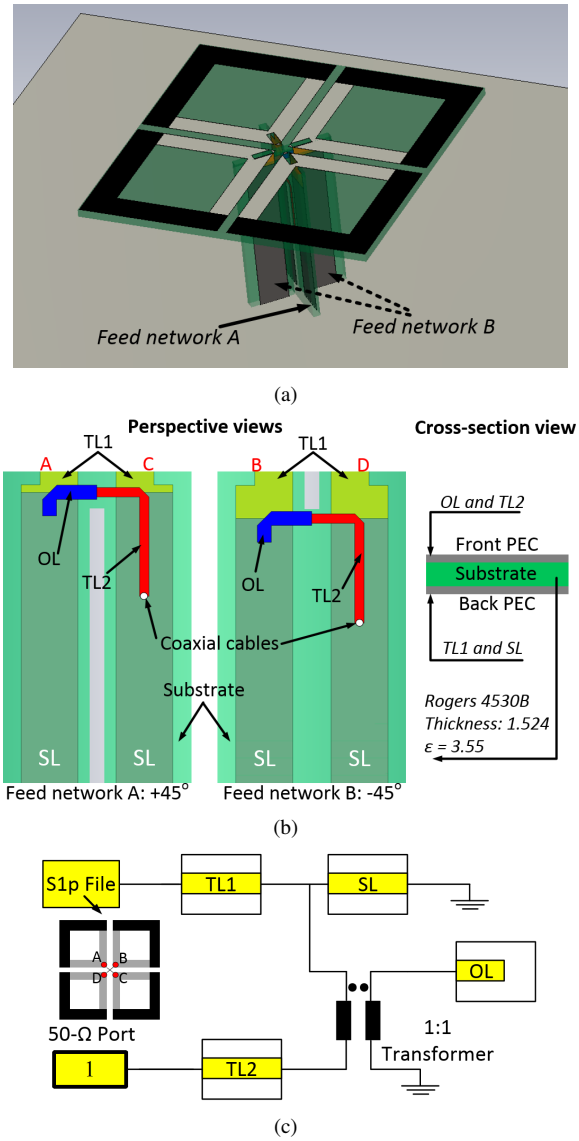

Fig. 14. Optimized simplified cross-dipole antenna. (a) Perspective view. (b) Details of the two feed networks implemented using PCBs. (c) Circuit theory model of the matching circuit.

TABLE III
OPTIMIZED DIMENSIONS OF THE TWO FEED NETWORKS
(DIMENSIONS IN MILLIMETERS)

Parameter	Feed A	Feed B	Description
W_SL	6.0	6.0	Width of the SL
L_SL	30.7	28.0	Length of the SL
W_TL1	6.0	6.0	Width of the TL1
L_TL1	2.4	5.1	length of the TL1
W_TL2	6.0	6.0	Width of the TL2
L_TL2	15.0	15.0	Length of the TL2
W_OL	6.0	6.0	Width of the OL
L_OL	1.5	1.5	Length of the OL
g	4.0	4.0	Separation distance between SL

the cross-dipole aperture. A matching circuit was implemented using microstrip technology. Two feed networks were designed to excite the two polarization states; they are depicted in Fig. 14(b). Note that TL2 and OL are conventional microstrip lines.

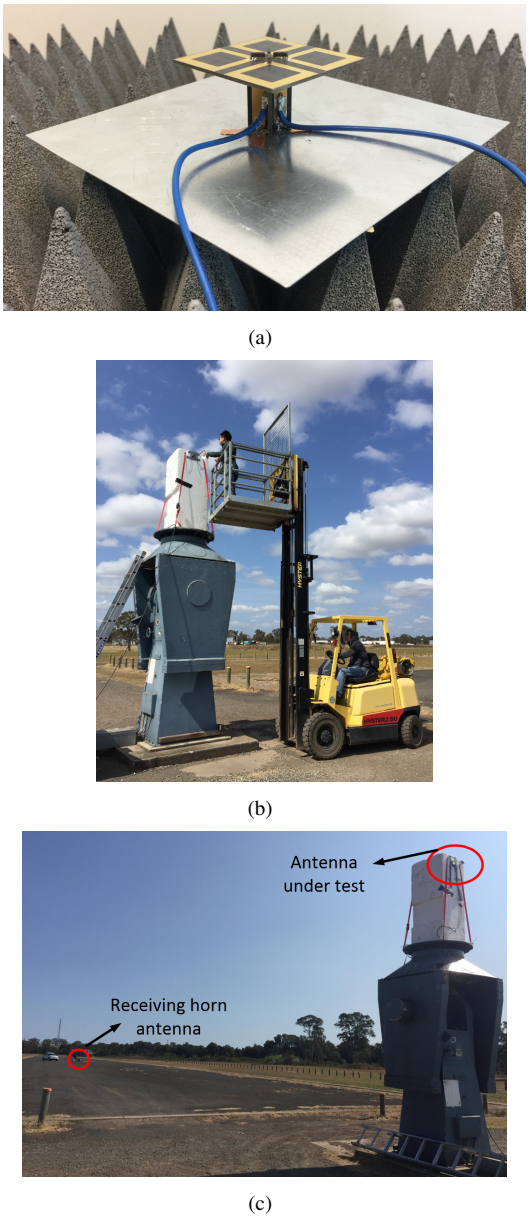

Fig. 15. Photos of the antenna and measurement system. (a) Fabricated and assembled antenna prototype. (b) Mounting the antenna. (c) Antenna under test (AUT).

They are designed on the front conducting layer. The lines TL1 and SL are realized as coupled lines printed on the back conducting layer. They not only form a balun to provide a balanced feed, but they also act as the ground planes for the microstrip lines TL2 and OL. This implementation results in a compact structure. The coaxial cables of the 50 Ω source are connected to the ends of TL2.

As shown in Fig. 14(c), the S1p file representing the input impedance between points A and C (or points B and D) was extracted from the full-wave simulation software CST Microwave Studio 2016. It was connected with the depicted ideal matching circuit in the MWS circuit simulator. The matching circuit consists of two segments of transmission lines TL1 and TL2, a short circuit transmission line SL, and an open circuit transmission line OL. Together with the cross-dipole

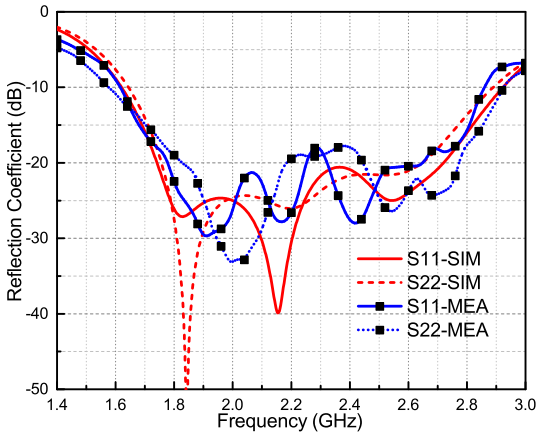

Fig. 16. Simulated and measured reflection coefficients of the two ports.

itself, the matching circuit acts like a ladder-type filter. The working mechanisms of this matching circuit are described in [17]. By optimizing the parameters of the transmission lines, excellent matching was achieved. The optimized dimension values of the feed networks are listed in Table III.

B. Results

The antenna was fabricated and tested. Fig. 15 shows the pictures of the antenna prototype and the test arrangement. The performance characteristics of the antenna were measured with an outdoor antenna range owned by Vecta Pty Ltd [18], located in Castle Hill, Sydney, Australia.

Plots of the simulated and measured reflection coefficients at the two ports as functions of the source frequency are shown in Fig. 16. The achieved impedance bandwidth with return loss < -15 dB is 1.1 GHz from 1.7 GHz to 2.8 GHz, which is even wider than the target bandwidth. Note that there is a slight difference between the $|S_{11}|$ and $|S_{22}|$ values. This is due to the fact that the two feed networks were designed not to be exactly the same as shown in Fig. 14(b). This choice avoids cross-talk between them. The co- and cross-polarization radiation patterns of the $-45°$-polarized cross-dipole at 1.7, 2.2, and 2.7 GHz are shown in Figs. 17(a), 17(b), and 17(c), respectively. The radiation patterns of the $+45°$-polarized cross-dipole are not given since those results are essentially the same. Fig. 18 illustrates the simulated and measured HPBWs of the two polarization states. They share a similar pattern, but a noticeable discrepancy at higher frequencies is observed. It is attributed mainly to the antenna fabrication and assembling errors. Despite this, the achieved HPBWs are quite stable and can meet the general industrial requirements. According to the measured results, the XPD at the boresight is > 20 dB and the lowest XPD level within the main beam ($-60° < \theta < 60°$) is > 8 dB. The measured XPD levels are lower than the simulated results. According to the engineer associated with Vecta's outdoor antenna range, the observed higher measured cross polarization levels are simply due to the imperfect ground plane (earth). The measured front-to-back ratio (FBR) is > 20 dB across this band. The measured realized gain varies from 7.3 to 8.2 dBi, which agrees very

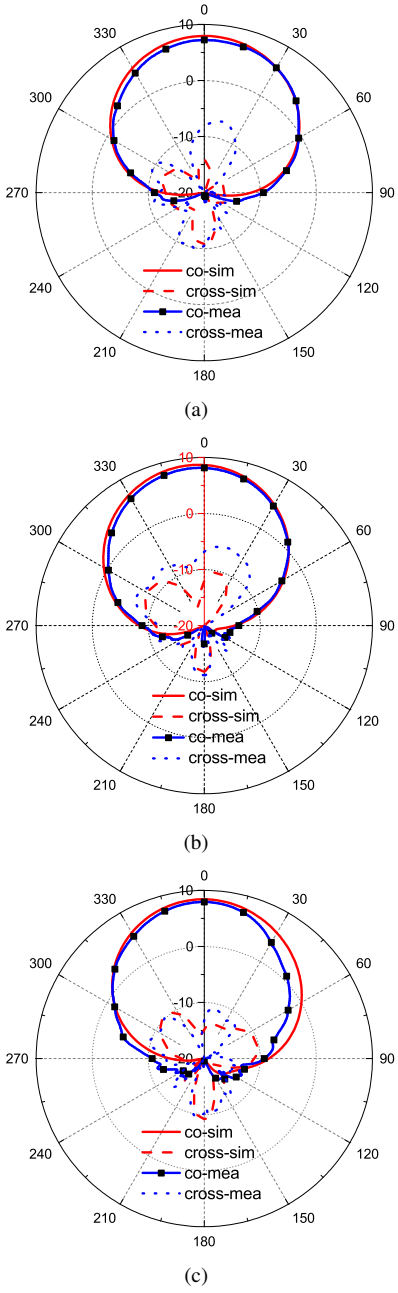

Fig. 17. Simulated and measured co- and cross-polarization radiation patterns at (a) 1.7, (b) 2.2, and (c) 2.7 GHz.

well with the simulated values. The corresponding simulated radiation efficiency values are above 81% across the entire band.

VI. Conclusion

A dual-polarized tightly-coupled cross-dipole system, such as those widely used in current 2G/3G/4G base stations, was analyzed. For the first time a deep insight into how this type of antenna works was given by decomposing the cross-dipole into two equivalent dipole arrays. By observing and studying the current distributions on the simplified model, it was found that the radiation performance of the system is determined by two terms: the patterns of the dipole arrays in the presence of

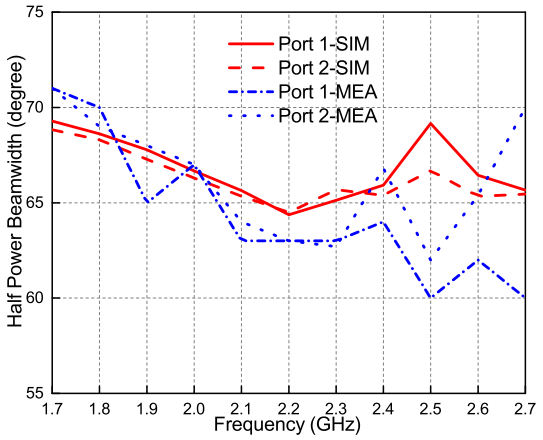

Fig. 18. Simulated and measured HPBW for the two polarizations across the target band.

the ground plane reflector and their array factor pattern. The interaction between these two factors makes the cross-dipole system achieve a very stable radiation performance, which is a requirement for all commercial base station applications. A design strategy based on a novel simplified dipole array model was introduced and validated.

An optimized cross-dipole system was synthesized following this design strategy. Low $|S_{11}|$ values, < -15 dB, were obtained along with excellent radiation performance. A prototype antenna based on this design was fabricated and tested. The measured performance characteristics were in very good agreement with their simulated values.

The knowledge generated from this work not only provides useful guidance for designing base station systems for current wireless networks, but it also can be applied to the design of future 5G base station antennas. We anticipate that the latter application may benefit the most from the enhanced understanding and validated design strategies presented in this article.

REFERENCES

[1] Y. Jin and Z. Du, "Broadband Dual-Polarized F-Probe Fed Stacked Patch Antenna for Base Stations," *IEEE Antennas and Wireless Propagation Letters*, vol. 14, pp. 1121-1124, 2015.

[2] Y. Gou, S. Yang, Q. Zhu and Z. Nie, "A Compact Dual-Polarized Double E-Shaped Patch Antenna With High Isolation," *IEEE Transactions on Antennas and Propagation*, vol. 61, no. 8, pp. 4349-4353, Aug. 2013.

[3] B. Q. Wu and K. M. Luk, "A Broadband Dual-Polarized Magneto-Electric Dipole Antenna With Simple Feeds," *IEEE Antennas and Wireless Propagation Letters*, vol. 8, pp. 60-63, 2009.

[4] K. M. Luk and B. Wu, "The Magnetoelectric Dipole – A Wideband Antenna for Base Stations in Mobile Communications," *Proceedings of the IEEE*, vol. 100, no. 7, pp. 2297-2307, July 2012.

[5] R. Lian, Z. Wang, Y. Yin, J. Wu and X. Song, "Design of a Low-Profile Dual-Polarized Stepped Slot Antenna Array for Base Station," *IEEE Antennas and Wireless Propagation Letters*, vol. 15, pp. 362-365, 2016.

[6] S. X. Ta, I. Park and R. W. Ziolkowski, "Crossed Dipole Antennas: A review," *IEEE Antennas and Propagation Magazine*, vol. 57, no. 5, pp. 107-122, Oct. 2015.

[7] H. D. Hristov, H. Carrasco, R. Feick, and B. L. Ooi, "Low-profile X antenna with flat reflector for polarization diversity applications," *Microwave and Optical Technology Letters*, vol. 51, pp. 1508-1512, 2009.

[8] Daoyi Su, J. J. Qian, Hua Yang and D. Fu, "A novel broadband polarization diversity antenna using a cross-pair of folded dipoles," *IEEE Antennas and Wireless Propagation Letters*, vol. 4, pp. 433-435, 2005.

[9] B. B. Jones and J. K. A. Allan, "Ultra-Wideband Dual-Band Cellular Base Station Antenna," US Patent 2014/0139387 A1, May, 2014.

[10] Q. X. Chu, D. L. Wen and Y. Luo, "A Broadband ±45° Dual-Polarized Antenna With Y-Shaped Feeding Lines," *IEEE Transactions on Antennas and Propagation*, vol. 63, no. 2, pp. 483-490, Feb. 2015.

[11] Z. Bao, Z. Nie and X. Zong, "A Novel Broadband Dual-Polarization Antenna Utilizing Strong Mutual Coupling," *IEEE Transactions on Antennas and Propagation*, vol. 62, no. 1, pp. 450-454, Jan. 2014.

[12] Y. Cui, R. Li and H. Fu, "A Broadband Dual-Polarized Planar Antenna for 2G/3G/LTE Base Stations," *IEEE Transactions on Antennas and Propagation*, vol. 62, no. 9, pp. 4836-4840, Sept. 2014.

[13] Y. Gou, S. Yang, J. Li and Z. Nie, "A Compact Dual-Polarized Printed Dipole Antenna With High Isolation for Wideband Base Station Applications," *IEEE Transactions on Antennas and Propagation*, vol. 62, no. 8, pp. 4392-4395, Aug. 2014.

[14] H. D. Hristov, H. Carrasco, R. Feick, and G. S. Kirov, "Broadband two-port X antenna array with flat reflector for polarization diversity applications," *Microwave and Optical Technology Letters*, vol. 52, pp. 2833-2837, Dec. 2010.

[15] H. Huang, Y. Liu, and S. X. Gong, "A Broadband Dual-Polarized Base Station Antenna With Anti-Interference Capability," *IEEE Antennas and Propagation Letters*, vol. 16, pp. 613-616, Mar. 2017.

[16] D. Z. Zheng and Q. X Chu, "A Multimode Wideband ±45° Dual-Polarized Antenna With Embedded Loops," *IEEE Antennas and Propagation Letters*, vol. 16, pp. 613-616, Mar. 2017.

[17] C. Ding, B. B. Jones, Y. J. Guo, and P.-Y. Qin, "Wideband Matching of Full-Wavelength Dipole with Reflector for Base Station, " *IEEE Transactions on Antennas and Propagation*, early access.

[18] Vectalabs. September 22, 2017 [Online], Available: http://vectalabs.com.